

1 INTRODUCTION

2 Above Earth's atmosphere are the Van Allen radiation belts, a toroidally-shaped
3 pair of belts that consist of a complex and dynamic plasma environment. The inner
4 radiation belt consists of mostly energetic protons, is very stable on year time scales,
5 and is located within 2 Earth radii (measured near the equator) above Earth's Earth's
6 surface. The outer radiation belt, on the other hand, consists of mostly energetic
7 electrons, is highly dynamic on day, and even hour time scales, and is typically
8 found between 4 and 8 Earth radii above Earth's surface. The radiation belts pose a
9 challenge to space exploration due to their effects on our technology-driven society.
10 Some of the effects include: a higher radiation dose for astronauts and cosmonauts,
11 degradation of silicon to the point where transistors malfunction, computer memory
12 corrupts due to bit flips, etc. With these effects in mind, it is no surprise that the
13 radiation belts have been extensively studied since their discovery in the 1960s.

14 The radiation belt plasma is at times unstable which in turn generate electric and
15 magnetic waves. These waves in turn accelerate and scatter radiation belt particles
16 with a variety of wave-particle mechanisms. One form of wave-particle interactions
17 scatter particles into Earth's atmosphere in the form of electron microbursts.

18 Electron microbursts, henceforth referred to as microbursts, are typically
19 observed by low Earth orbiting spacecraft, sounding rockets, and high altitude
20 balloons as a sub-second impulse of electrons. Some of the most intense microbursts
21 have electron fluxes that are a factor of 10 to 100 above the background (for example
22 see Fig. 7 in Blake et al. (1996)). Since they were first reported by Anderson and
23 Milton (1964), the intense transient nature of microbursts have compelled countless
24 researchers to understand their properties, their effects on the environment, and the
25 physical mechanism(s) that create microbursts. Microbursts are widely believed

26 to be created by wave-particle scattering between a plasma wave called whistler
 27 mode chorus and outer radiation belt electrons, although many details regarding the
 28 scattering mechanism are unconstrained or unknown. The goal of this dissertation is
 29 to study the wave-particle scattering mechanism that scatters electron microbursts.

30 This chapter serves as an introduction to the fundamental physical concepts
 31 that are essential to understand wave-particle interactions in Earth's magnetosphere.
 32 We will first derive the motion of individual charged particles in Earth's electric and
 33 magnetic fields. Next we will cover how various groups of charged particles coalesce
 34 to form the major particle populations in the magnetosphere. Then, we will cover
 35 the various mechanisms that accelerate and scatter particles in the magnetosphere.
 36 Lastly, we will review the basics of microbursts as a jumping-off point for the rest of
 37 the dissertation.

38 Charged Particle Motion in Electric and Magnetic Fields

A charged particle trapped in the magnetosphere will experience three types of periodic motion in Earth's nearly dipolar magnetic field. The three motions are ultimately due to the Lorentz force that a particle of momentum \vec{p} , charge q , and velocity \vec{v} experiences in an electric field \vec{E} and magnetic field \vec{B} and is given by

$$\frac{d\vec{p}}{dt} = q(\vec{E} + \vec{v} \times \vec{B}). \quad (1.1)$$

39 In the magnetosphere, the three periodic motions, in decreasing frequency, are
 40 gyration, bounce, and drift and are schematically shown in Fig. 1.1. Each of periodic
 41 these motions have a corresponding conserved quantity i.e. an adiabatic invariant.

The highest frequency periodic motion is gyration about a magnetic field of

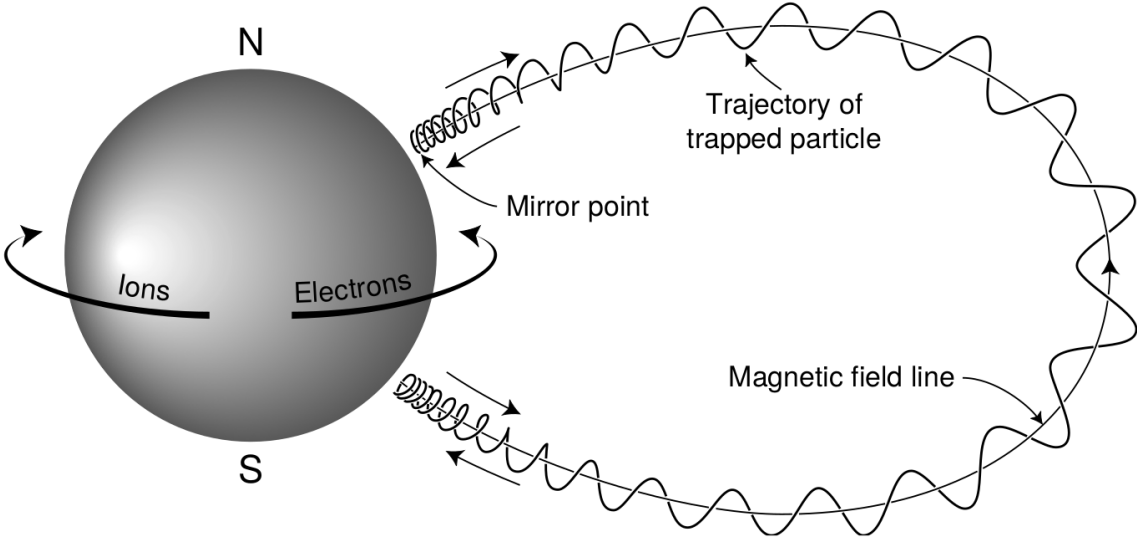


Figure 1.1: The three periodic motions of charged particles in Earth's dipole magnetic field. These motions are: gyration about the magnetic field line, bounce motion between the magnetic poles, and azimuthal drift around the Earth. Figure from (Baumjohann and Treumann, 1997).

magnitude B . This motion is circular with a Larmor radius of

$$r = \frac{mv_{\perp}}{|q|B} \quad (1.2)$$

where m is the mass and v_{\perp} the particle's velocity perpendicular to \vec{B} . This motion has a corresponding gyrofrequency

$$\Omega = \frac{|q|B}{m} \quad (1.3)$$

in units of radians/second. Inside the radiation belts the electron gyrofrequency, Ω_e is on the order of a kHz. The corresponding adiabatic invariant is found by integrating the particle's canonical momentum around the particle's path of gyration

$$J_i = \oint (\vec{p} + q\vec{A}) \cdot d\vec{l} \quad (1.4)$$

42 where J_i is the i^{th} adiabatic invariant and \vec{A} is the magnetic vector potential. This
 43 integral is carried out by integrating the first term over the circumference of the gyro
 44 orbit and integrating the second term using Stokes theorem to calculate the magnetic
 45 flux enclosed by the gyro orbit. The gyration invariant is then $J_1 \sim v_{\perp}^2/B$, which is
 46 conserved when the frequency, ω of a force acting on the gyrating electron satisfies
 47 $\omega \ll \Omega_e$.

48 The second highest frequency periodic motion is bouncing due to a parallel
 49 gradient in \vec{B} . This periodic motion naturally arises in the magnetosphere because
 50 Earth's magnetic field is stronger near the poles, and artificially in the laboratory
 51 in magnetic bottle machines. To understand this motion we first we need to define
 52 the concept of pitch angle α as the angle between \vec{B} and \vec{v} which is schematically
 53 shown in Fig. 1.2a. The pitch angle relates v with v_{\perp} , and v_{\parallel} (the component of the
 54 particles velocity parallel to \vec{B}). As shown in 1.2b and c, a smaller (larger) α will
 55 increase (decrease) the distance that the charged particle travels parallel to \vec{B} , during
 56 one gyration.

Assuming the particle's kinetic energy is conserved, the conservation of J_1
 implies that given a particle's $v_{\perp}(0)$ and $B(0)$ at the magnetic equator (where Earth's
 magnetic field is usually at a minimum), we can calculate its $v_{\perp}(s)$ along the particle's
 path s by calculating $B(s)$ from magnetic field models. The particle's perpendicular
 velocity is then related via

$$\frac{v_{\perp}^2(0)}{B(0)} = \frac{v_{\perp}^2(s)}{B(s)} \quad (1.5)$$

57 which can be rewritten as

$$\frac{v^2 \sin^2 \alpha(0)}{B(0)} = \frac{v^2 - v_{\parallel}^2(s)}{B(s)} \quad (1.6)$$

⁵⁸ and re-arranged to solve for $v_{||}(s)$

$$v_{||}(s) = v \sqrt{1 - \frac{B(s)}{B(0)} \sin^2 \alpha(0)} \quad (1.7)$$

⁵⁹ which will tend towards 0 when the second term in the radical approaches 1.

⁶⁰ The location where $v_{||}(s) = 0$ is called the mirror point and is where a particle
⁶¹ reverses direction. Since Earth's magnetic field is stronger towards the poles, the
⁶² mirroring particle will execute periodic bounce motion between its two mirror points
⁶³ in the northern and southern hemispheres. The corresponding adiabatic invariant, J_2
⁶⁴ is

$$J_2 = \oint p_{||} ds \quad (1.8)$$

where ds describes the particle path between the mirror points in the northern and southern hemispheres (see Fig. 1.1). J_2 is found by substituting Eq. 1.7 into Eq. 1.8 and defining the magnetic field strength at the mirror points as B_m where $\alpha(m) = 90^\circ$.

The J_2 integral can be written as

$$J_2 = 2p \int_{m_n}^{m_s} \sqrt{1 - \frac{B(s)}{B(m)}} ds \quad (1.9)$$

⁶⁵ where m_n and m_s are the northern and southern mirror points, respectively. The
⁶⁶ bounce period can be estimated (e.g. Baumjohann and Treumann, 1997) to be

$$t_b \approx \frac{LR_e}{\sqrt{W/m}} (3.7 - 1.6 \sin \alpha(0)) \quad (1.10)$$

⁶⁷ where L is the L -shell which describes the distance from the Earth's center to the
⁶⁸ location where a particular magnetic field line crosses the magnetic equator, in units
⁶⁹ of Earth radii, R_e . W is the particle's kinetic energy. As with gyration, the particle

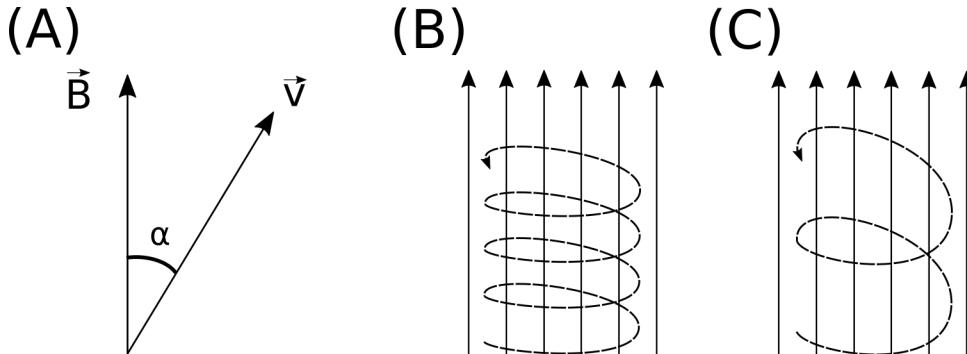


Figure 1.2: Charged particle motion in a uniform magnetic field \vec{B} . Panel (A) shows the geometry defining the pitch angle, α . Panel (B) and (C) show two helical electron trajectories with dashed lines assuming a large and small α (corresponding to a small and large parallel velocity $v_{||}$), respectively.

70 will bounce between the mirror points as long as $\omega \ll \Omega_b$, where Ω_b is the bounce
71 frequency.

72 At this stage it is instructional to introduce the notion of the loss cone pitch
73 angle, α_L . A particle with $\alpha \leq \alpha_L$ will mirror at or below ≈ 100 km altitude in
74 the atmosphere. A charged particle gyrating at those altitudes will encounter and
75 Coulomb scatter with the dense atmosphere and be lost from the magnetosphere.

76 The slowest periodic motion experienced by charged particles in Earth's mag-
77 netic field is azimuthal drift around the Earth. This drift results from a combination of
78 a radial gradient in \vec{B} and the curvature of the magnetic field. The radial gradient drift
79 arises because Earth's magnetic field is stronger near the Earth where the particle's
80 gyroradius radius of curvature is smaller as it gyrates towards stronger magnetic field,
81 and larger when it gyrates outward. The overall effect is the particle gyro orbit does
82 not close on itself and negatively charged particles drift east and positively charged
83 particles drift west. The radial gradient drift is enhanced by the centrifugal force that
84 a particle experiences as it bounces along the curved field lines. The drift adiabatic
85 invariant, J_3 is found by integrating Eq. 1.4 over the complete particle orbit around

86 the Earth. The shape of this drift orbit is otherwise known as a drift shell. For J_3 ,
 87 the first term is negligible and the second term is the magnetic flux enclosed by the
 88 drift shell, Φ_m i.e. $J_3 \sim \Phi_m$.

89 Figure 1.3 from Schulz and Lanzerotti (1974) shows contours of the gyration,
 90 bounce, and drift frequencies for electrons and protons in Earth's dipole magnetic
 91 field.

Up until now we have considered the three periodic motions due Earth's magnetic field and the absence of electric fields. If \vec{E} is present, a particle's center of gyration i.e., averaged position of the particle over a gyration, will drift with a velocity perpendicular to both \vec{E} and \vec{B} . The drift velocity can be solved directly from Eq. 1.1 and is

$$\vec{v}_E = \frac{\vec{E} \times \vec{B}}{B^2}. \quad (1.11)$$

92 Lastly, for more detailed derivations of these motions, see the following texts:
 93 Baumjohann and Treumann (1997); Schulz and Lanzerotti (1974); Tsurutani and
 94 Lakhina (1997).

95 Particle Populations and Their Interractions in the Magnetosphere

96 Now that we have looked at the dynamics of single-particle motion in electric
 97 and magnetic fields, we will briefly tour the various macroscopic populations in the
 98 magnetosphere that are illustrated in Fig. 1.4.

99 The sun and its solar wind are ultimately the source of energy input into the
 100 magnetosphere. The solar wind at Earth's orbit is a plasma traveling at supersonic
 101 speeds with an embedded interplanetary magnetic field (IMF). When the solar wind
 102 encounters Earth's magnetic field, the plasma can not easily penetrate into the
 103 magnetosphere because the plasma is frozen-in on magnetic field lines. Thus the

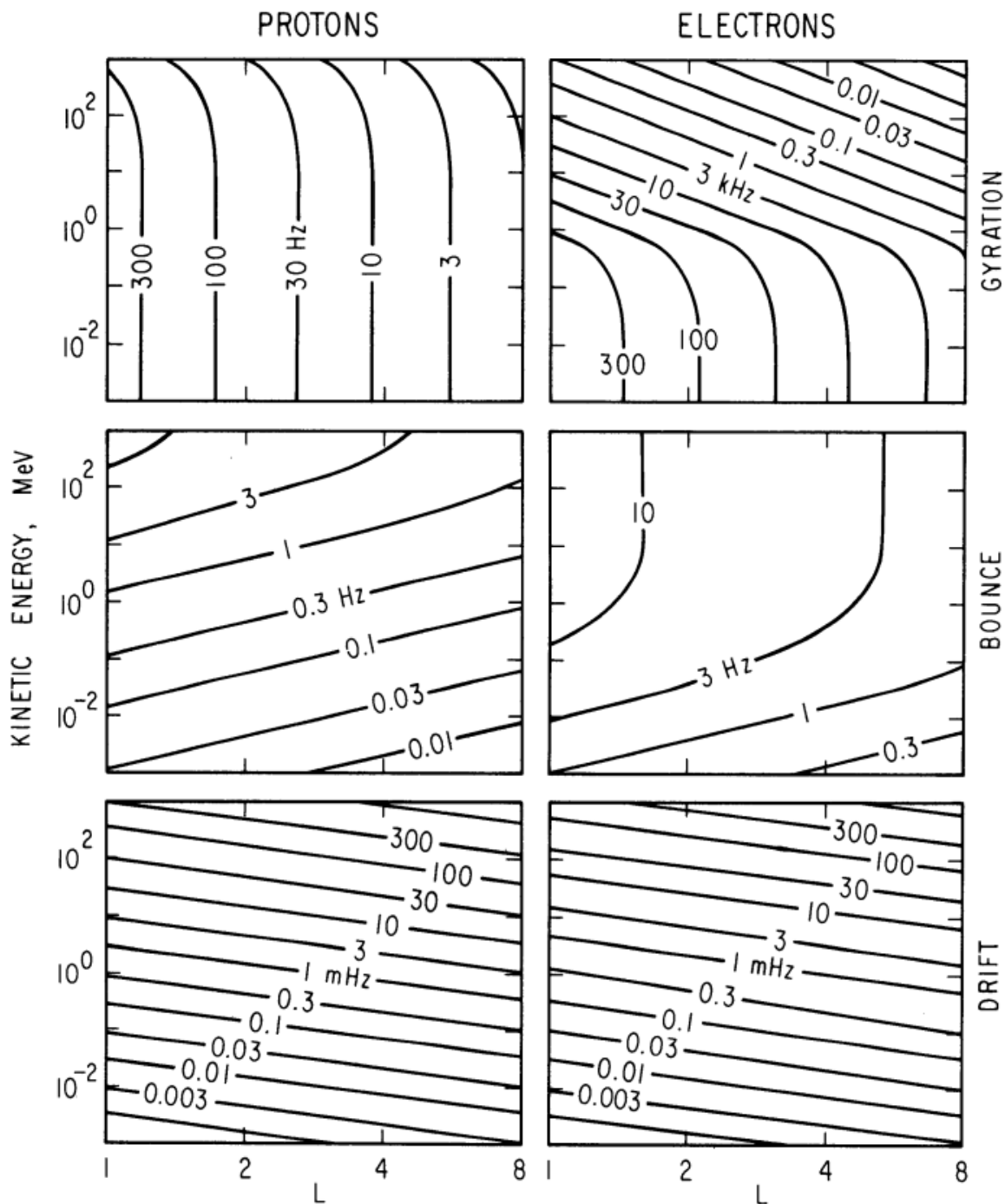


Figure 1.3: Contours of constant gyration, bounce, and drift frequencies for electrons and protons in a dipole field. Figure from Schulz and Lanzerotti (1974).

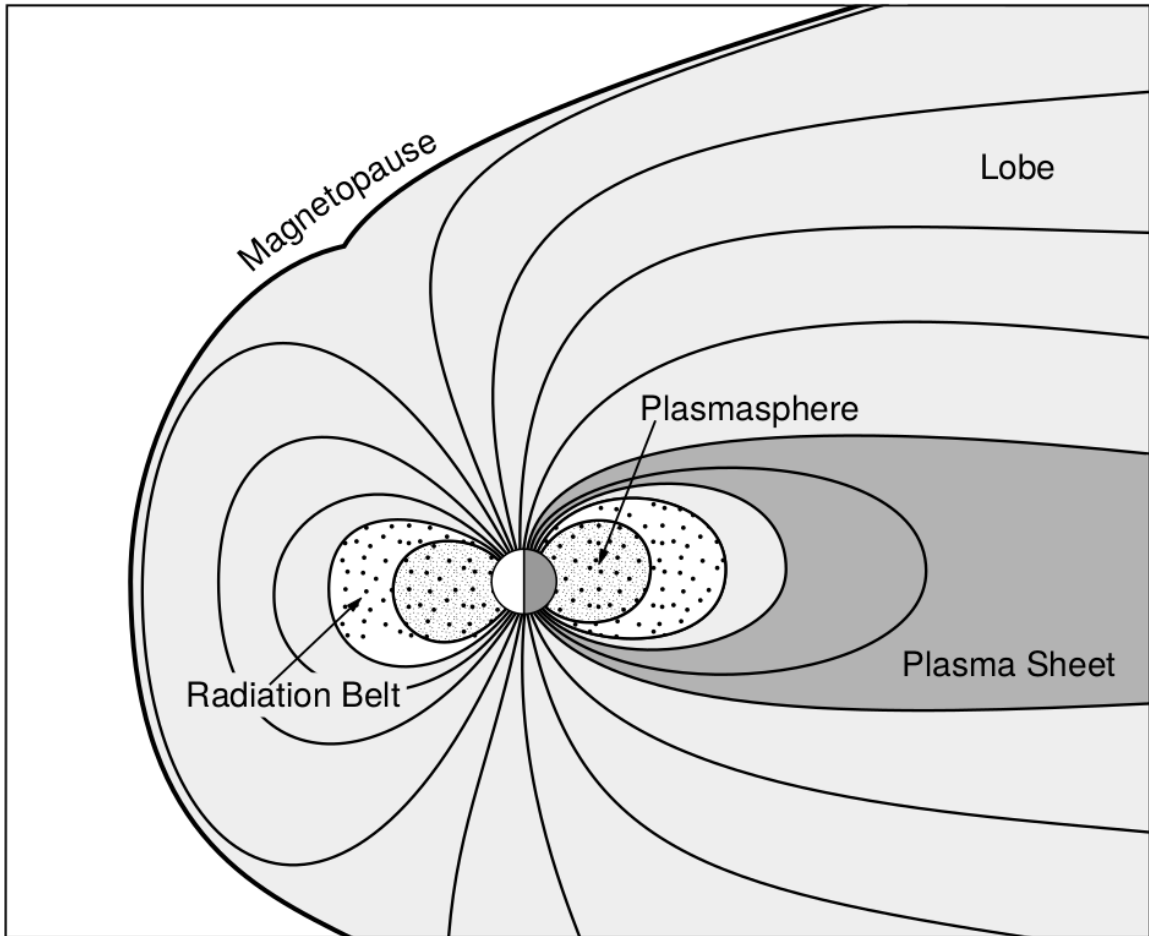


Figure 1.4: Macroscopic structures in the inner magnetosphere most relevant to this dissertation. The plasmasphere, and the radiation belts are shown and ring current is co-located there as well. Figure from Baumjohann and Treumann (1997).

104 plasma and its magnetic field drapes around the magnetosphere forming a cavity in
 105 the solar wind that is roughly shaped as shown in Fig. 1.4. Because the solar wind
 106 is supersonic at 1 AU, a bow shock exists upstream of the magnetosphere. The solar
 107 wind plasma, after it is shocked by the bow shock, flows around the magnetosphere
 108 inside the magnetosheath. The surface where the solar wind ram pressure and Earth's
 109 magnetic pressure balance is termed the magnetopause, which can be thought of as
 110 a boundary between the solar wind's and Earth's plasma environments. This is
 111 a slightly naive description of the magnetopause, but is nonetheless an instructive
 112 conceptual picture. The shocked plasma then flows past the Earth where it shapes
 113 the magnetotail. In the magnetotail the solar wind magnetic pressure balances Earth's
 114 magnetic field pressure in the lobes. The magnetotail extends on the order of 100
 115 R_E downstream of Earth, and the tailward stretching of magnetic field lines creates
 116 the plasma sheet which exists in the region of low magnetic field strength near the
 117 magnetic equator (e.g. Eastwood et al., 2015).

118 Populations in the Inner Magnetosphere

119 Closer to Earth, where the magnetic field is largely dipolar, are three plasma
 120 populations that comprise the inner magnetosphere: the plasmasphere, the ring
 121 current, and the radiation belts. Before we describe these three particle populations
 122 in detail, we will first introduce the coordinate system that most naturally describes
 123 the inner magnetosphere environment, and the electric fields that affect mostly low
 124 energy particles.

125 In this coordinate system the “radial” coordinate was defined in section 1 and
 126 is the L shell. The azimuthal coordinate is the magnetic local time (MLT). For an
 127 observer above Earth's north pole looking down, MLT is defined to be 0 (midnight)
 128 in the anti-sunward direction, and increases in the counter-clockwise direction with 6

at dawn, 12 at noon (sunward direction), and 18 in dusk. The final coordinate is the magnetic latitude, λ which is analogous to the latitude coordinate in the spherical coordinate system, and is defined to be 0 at the magnetic equator. This coordinate system naturally describes the following inner magnetosphere populations.

The low energy particle dynamics in the inner magnetosphere are organized by two electric fields: the co-rotation and the dawn-dusk electric fields. The co-rotation electric field arises from the rotation of Earth's magnetic field. Since particles are frozen on magnetic field lines and the plasma conductivity is effectively infinite, to a non-rotating observer, Earth's rotation appears as a radial electric field that drops off as $\sim L^2$. This electric field makes particles orbit around the Earth due to the $\vec{E} \times \vec{B}$ drift. The other electric field, pointing from dawn to dusk is called the convection electric field and is due to the Earthward transport of particles from the magnetotail that appears as an electric field to a stationary observer (with respect to Earth). The superposition of the co-rotation and convection electric fields results in a potential field shown in Fig. 1.5. The shaded area in Fig. 1.5 shows the orbits on which low energy electrons are trapped, and outside are the untrapped particles. The dynamic topology of the shaded region in Fig. 1.5 is controlled by only the convection electric field which is dependent on the solar wind speed and the IMF. The lowest energy particles, that are most effected by these electric fields, make up the plasmasphere.

Plasmasphere The plasmasphere is a dense ($n_e \sim 10^3/\text{cm}^3$), cool plasma ($\sim \text{eV}$) that extends to $L \sim 4$ (extent is highly dependent on the solar wind and magnetospheric conditions) and is sourced from the ionosphere. The two main mechanisms that source the cold plasma from the ionosphere are ultraviolet ionization by sunlight and particle precipitation. The ultraviolet ionization by sunlight is strongly dependent on the time of day (day vs night), latitude (more ionization near

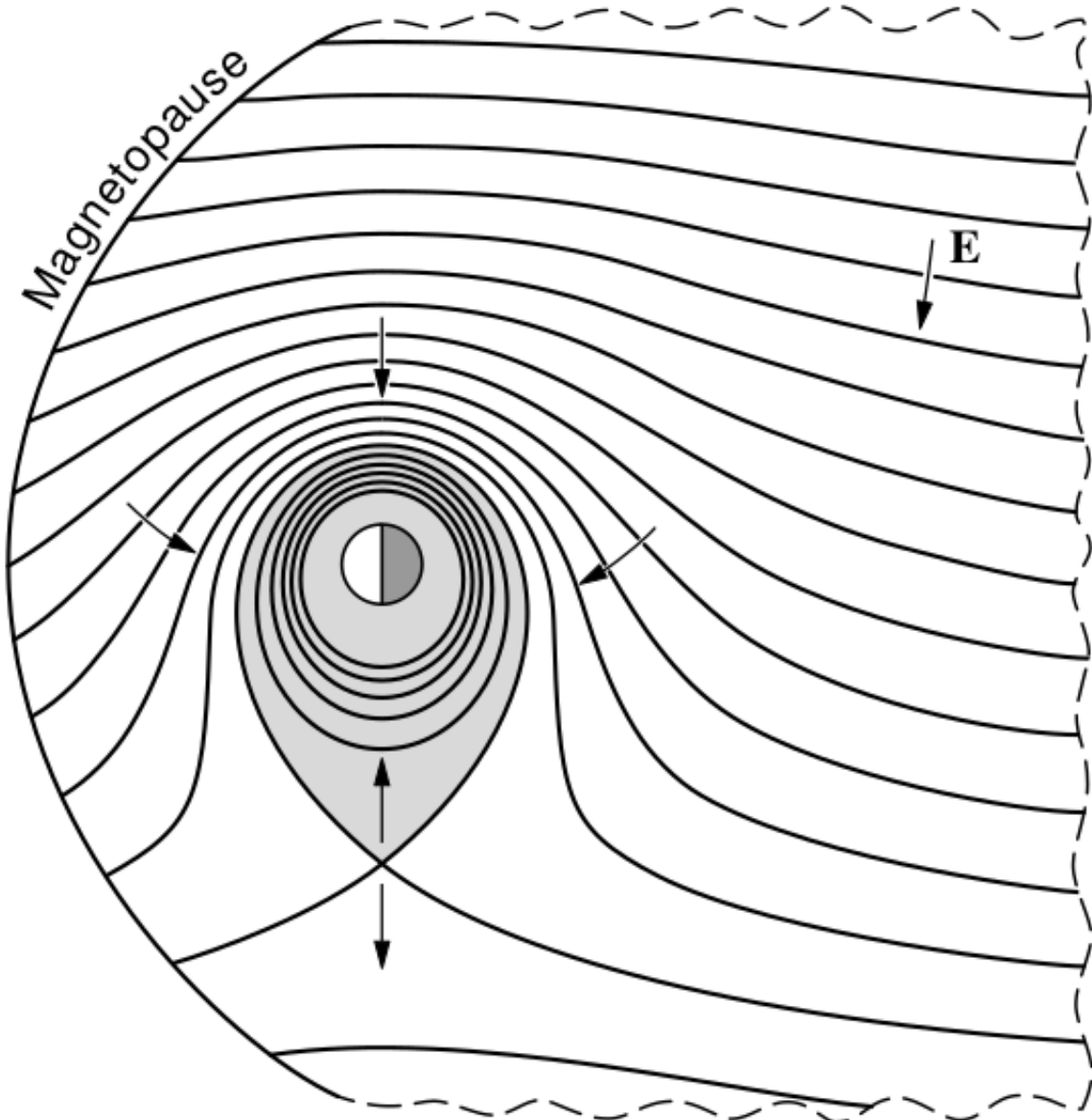


Figure 1.5: Equipotential lines and electric field arrows due to the superposition of the co-rotation and convection electric fields. Electrons in the shaded region execute closed orbits. Outside of the shaded regions the electrons are not trapped and will escape. The region separating the two regimes is called the Alfvén layer. Figure from Baumjohann and Treumann (1997).

154 the equator). The ionization due to particle precipitation, on the other hand, is highly
 155 dependent on magnetospheric conditions, and mostly occurs at high latitudes.

156 The outer boundary of the plasmasphere is the plasmapause which is typically
 157 identified as a steep radial gradient in plasma density from $\sim 10^3/\text{cm}^3$ to $\sim 1/\text{cm}^3$. As
 158 we will see throughout this dissertation, the location of the plasmapause is important
 159 to model (e.g. O'Brien and Moldwin, 2003) and understand since the plasma density
 160 strongly controls the efficiency of particle scattering (Horne et al., 2005).

161 Ring Current The next higher energy population is the ring current. This
 162 population consists of protons and electrons between tens and a few hundred keV
 163 that drift around the Earth. The orbits of higher energy particles are not as effected
 164 by the convection and co-rotation electric field, rather they drift around the Earth
 165 due to gradient and curvature drifts. Since the direction of the drift is dependent on
 166 charge, protons drift west around the Earth and electrons drift East. This has the
 167 effect of creating a current around the Earth.

168 The ring current generates a magnetic field which decreases the magnetic field
 169 strength on Earth's surface and increases it outside of the ring current. The decrease
 170 of Earth's magnetic field strength is readily observed by a system of ground-based
 171 magnetometers and is merged into a Disturbance Storm Time (DST) index. An
 172 example of a DST index time series from a coronal mass ejection (CME) driven 2015
 173 St. Patrick's Day storm is shown in Fig. 1.6. The ring current is sometimes first
 174 depleted and DST increases slightly (initial phase or sudden storm commencement).
 175 Then the ring current is rapidly built up during which DST rapidly decreases (main
 176 phase). Lastly the ring current gradually decays toward its equilibrium state over a
 177 period of a few days and DST increases towards 0 (recovery phase). The DST index
 178 along with other indicies are readily used by the space physics community to quantify

₁₇₉ the global state of the magnetosphere.

₁₈₀ Radiation Belts The highest energy particle populations are in the Van Allen
₁₈₁ radiation belts. These belts were discovered by Van Allen (1959) and Vernov and
₁₈₂ Chudakov (1960) during the Cold War and are a pair of toroidally shaped populations
₁₈₃ of trapped electrons and protons usually within to $L < 8$ and are shown in Fig. 1.7.
₁₈₄ Their quiescent toroidal shape is similar to the shape of the plasmasphere and ring
₁₈₅ current and is a result of Earth's dipole magnetic field and the conservation of the
₁₈₆ three adiabatic invariants discussed in section 1.

₁₈₇ The inner radiation belt is extremely stable on time periods of years, extends
₁₈₈ to $L \approx 2$, and mainly consists of protons with energies between MeV and GeV and
₁₈₉ electrons with energies up to ≈ 1 MeV (Claudepierre et al., 2019). The source of
₁₉₀ inner radiation belt protons is believed to be due to cosmic-ray albedo neutron decay
₁₉₁ (e.g. Li et al., 2017) and inward radial diffusion for electrons (e.g. O'Brien et al.,
₁₉₂ 2016). The gap between the inner and outer radiation belt is called the slot, which is
₁₉₃ believed to be due to hiss waves inside the plasmasphere (described below) scattering
₁₉₄ particles into the atmosphere (e.g. Breneman et al., 2015; Lyons and Thorne, 1973).

₁₉₅ The outer radiation belt, on the other hand is much more dynamic and consists
₁₉₆ of mainly electrons of energies up to a few MeV. The outer belt's spatial extent is
₁₉₇ highly variable e.g. see Fig. 1.8, and is typically observed at $4 < L < 8$. Since
₁₉₈ the outer radiation belt contains a dynamic population of energetic particles that
₁₉₉ pose a threat to human and technological presence in Earth's atmosphere and space,
₂₀₀ decades of research has been undertaken to understand and predict the outer radiation
₂₀₁ belt particles, waves, and wave-particle interactions. The dynamics of the outer
₂₀₂ radiation belt can be understood by considering various competing acceleration and
₂₀₃ loss mechanisms which will be described in the following sections.

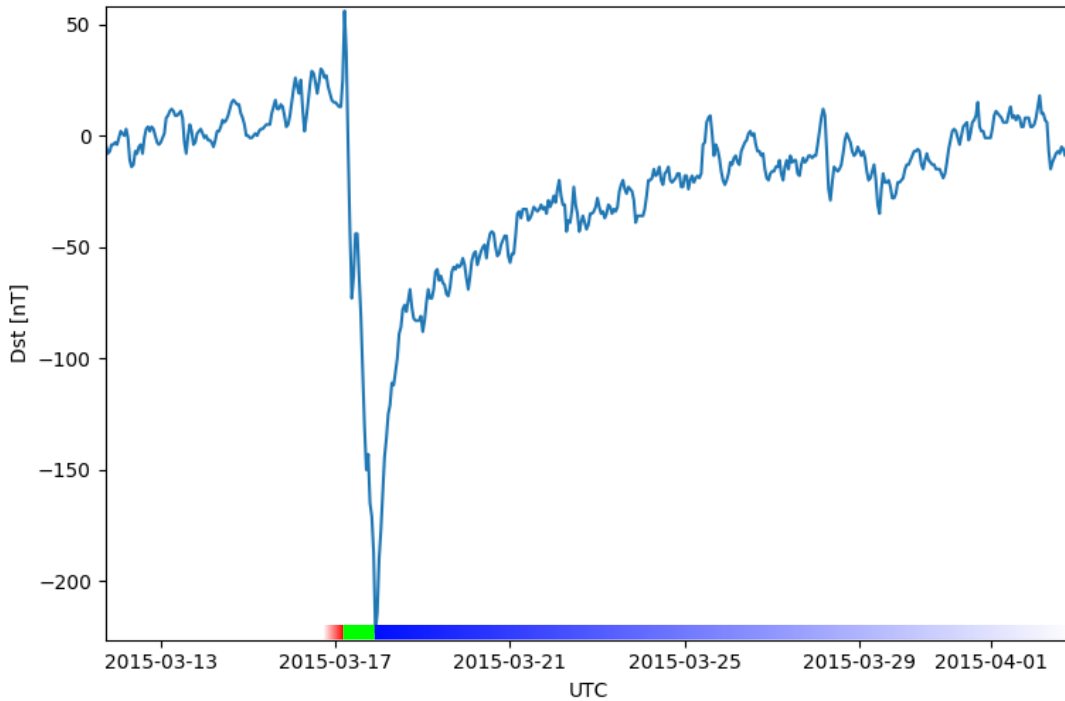


Figure 1.6: The DST index during the St. Patrick's Day 2015 storm. This storm was caused by a coronal mass ejection on March 15th, 2015. The storm phases are: initial phase, main phase, and recovery phase. The initial phase occurred when the Dst peaked at $+50$ nT on March 17th during which the ring current was eroded by the coronal mass ejection during the interval shown by the red bar. Then the rapid decrease to ≈ -200 nT was during the main phase where many injections from the magnetotail pumped up the ring current which reduced Earth's magnetic field strength at the ground and is shown with the green bar. Lastly, the recovery phase lasted from March 18th to approximately March 29th during which the ring current particles were lost and the ring current returned to its equilibrium state. The recovery phase is shown with the blue bar.

The Earth's Electron Radiation Belts

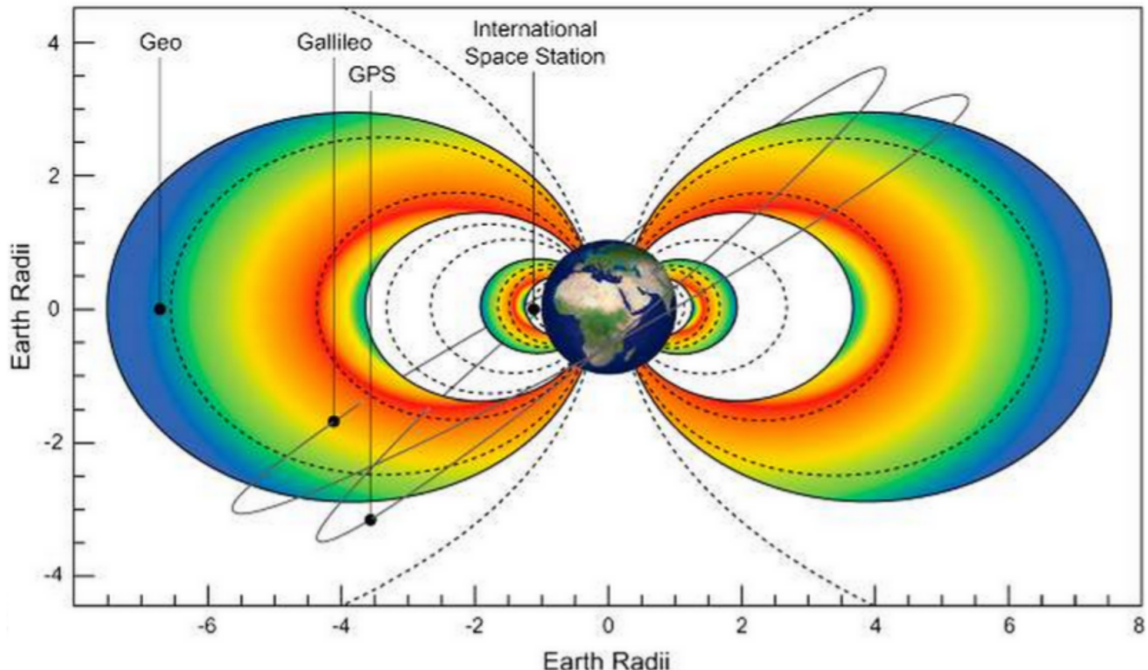


Figure 1.7: The two radiation belts with the locations of various satellites and orbits.
Figure from (Horne et al., 2013).

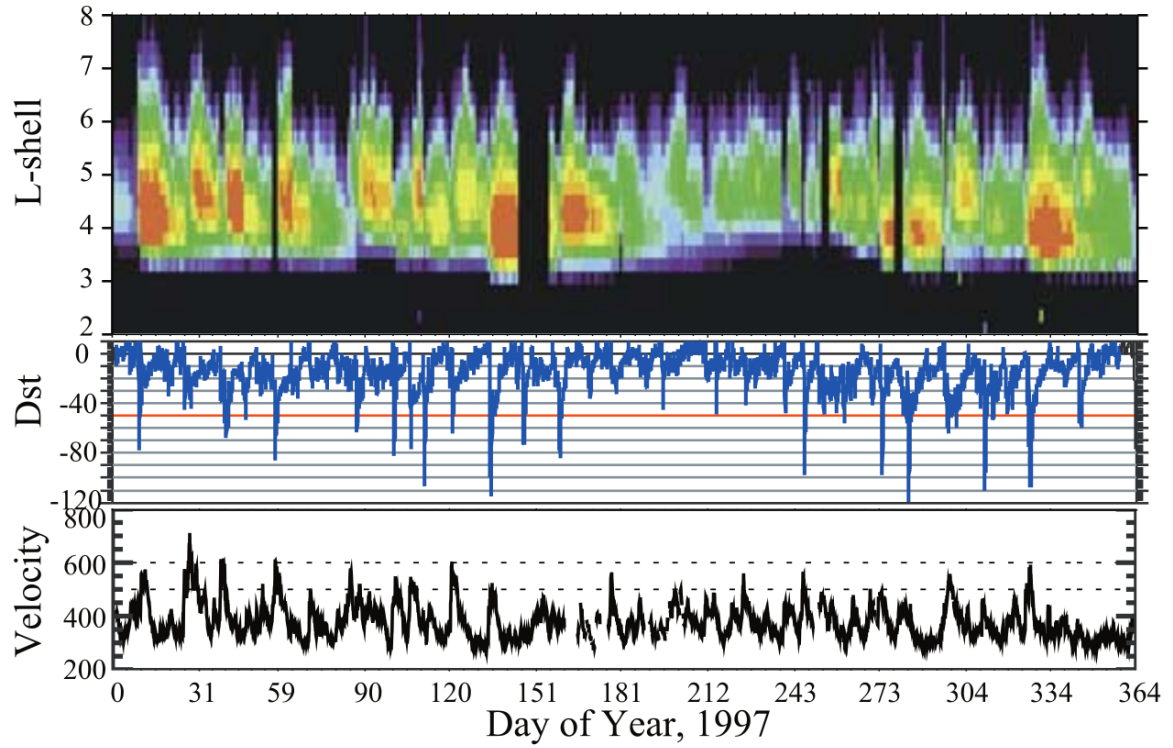


Figure 1.8: The dynamics of the outer radiation belt in 1997 from the POLAR satellite. Top panel shows the 1.2-2.4 MeV electron flux as a function of L and 1997 day of year. The middle panel shows the DST index, and bottom panel shows the solar wind velocity. Figure from (Reeves et al., 2003).

204

Radiation Belt Particle Sources and Sinks205 Adiabatic Heating

206 One of the particle heating and transport mechanisms arises from the Earthward
 207 convection of particles. The conservation of J_1 implies that the initial and final v_{\perp}
 208 depends on the change in the magnetic field amplitude

$$\frac{v_{\perp i}^2}{B_i} = \frac{v_{\perp f}^2}{B_f}. \quad (1.12)$$

209 As a particle convects Earthward, $B_f > B_i$ thus v_{\perp} must increase. The dipole
 210 magnetic field amplitude can be written as

$$B(L, \theta) = \frac{31.2 \mu\text{T}}{L^3} \sqrt{1 + 3 \cos^2 \theta} \quad (1.13)$$

211 which implies that

$$\frac{v_{\perp f}^2}{v_{\perp i}^2} = \left(\frac{L_i}{L_f} \right)^3. \quad (1.14)$$

212 .

213 In addition, as the particle convects Earthward the distance between the
 214 particle's mirror points decrease. If J_2 is conserved, the shrinking bounce path implies
 215 that $v_{||}$ must increase by

$$\frac{v_{|| f}^2}{v_{|| i}^2} = \left(\frac{L_i}{L_f} \right)^k \quad (1.15)$$

216 where k ranges from 2 for equatorial pitch angles, $\alpha_{eq} = 0^\circ$, to 2.5 for $\alpha_{eq} = 90^\circ$
 217 (Baumjohann and Treumann, 1997). Since the rate of adiabatic heating is greater in
 218 the perpendicular direction than heating in the parallel direction, an initially isotropic

219 particle distribution will become anisotropic during its convection. These isotropic
220 particles can then become unstable to wave growth and generate waves in order to
221 reach equilibrium.

222 Wave Resonance Heating

223 Another mechanism that heats particles is due to particles resonating with
224 plasma waves. A few of the electromagnetic wave modes responsible for particle
225 acceleration (and deceleration) relevant to radiation belt dynamics are hiss, whistler
226 mode chorus (chorus), and electromagnetic ion cyclotron (EMIC) waves. These waves
227 are created by the loss cone instability that driven by an anisotropy of electrons
228 for chorus waves, and protons for EMIC waves. The level of anisotropy can be
229 quantified by the ratio of the perpendicular to parallel particle temperatures (T_{\perp}/T_{\parallel}).
230 A particle distribution is unstable when $T_{\perp}/T_{\parallel} > 1$ which facilitates wave growth.
231 Since electrons gyrate in a right-handed sense, the chorus waves also tend to be right
232 hand circularly polarized (Tsurutani and Lakhina, 1997). The same argument applies
233 to protons and left hand circularly polarized EMIC waves as well.

234 These circularly polarized waves can resonate with electrons and/or protons
235 when their combined motion results in a static \vec{E} . One example of a resonance
236 between a right hand circularly polarized wave and an electron is shown in Fig. 1.21
237 and is termed the cyclotron resonance. An electron's v_{\parallel} and the wave's parallel wave
238 vector, k_{\parallel} are in opposite directions such that the wave frequency ω is Doppler shifted
239 to an integer multiple of the Ω_e at which point the electron feels a static electric
240 field and is accelerated or decelerated. This acceleration happens when a resonance
241 condition is satisfied between a wave and a particle for which we will now derive an
242 illustrative toy model.

243 Assume a uniform magnetic field $\vec{B} = B_0 \hat{z}$ with a parallel propagating ($k = k \hat{z}$),

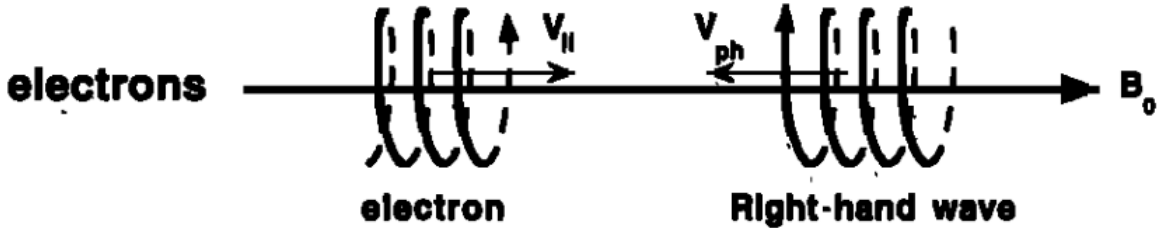


Figure 1.9: The trajectories of an electron and a right-hand circularly polarized wave during a cyclotron resonance. The electron's v_{\parallel} and the wave's k_{\parallel} are in opposite directions such that the wave's frequency is Doppler shifted to an integer multiple of the electron cyclotron frequency. Figure from (Tsurutani and Lakhina, 1997).

²⁴⁴ right-hand circularly polarized wave. The wave's electric field as a function of position
²⁴⁵ and time can be written as

$$\vec{E} = E_0(\cos(\omega t - kz)\hat{x} + \sin(\omega t - kz)\hat{y}) \quad (1.16)$$

which is more clearly expressed by taking the dot product to find \vec{E} in the $\hat{\theta}$ direction

$$E_{\theta} = \vec{E} \times \hat{\theta} = E_0 \cos(\omega t - kz + \theta). \quad (1.17)$$

²⁴⁶ Now assume that the electron is traveling in the $-\hat{z}$ direction with a velocity $\vec{v} = -v_0\hat{z}$
²⁴⁷ so its time dependent position along \hat{z} is

$$z(t) = -v_0 t \quad (1.18)$$

²⁴⁸ and gyrophase is

$$\theta(t) = -\Omega t + \theta(0) \quad (1.19)$$

²⁴⁹ where the first negative sign comes from the electron's negative charge. Now we put

250 this all together and express the electric field and the force that the electron will
 251 experience

$$m \frac{dv_\theta}{dt} = qE_\theta = qE_0 \sin((\omega + kv_0 - \Omega)t + \theta(0)). \quad (1.20)$$

252 This is a relatively complex expression, but when the time dependent component,

$$\omega + kv_0 - \Omega = 0, \quad (1.21)$$

253 the electron will be in a static electric field which will accelerate or decelerate the
 254 electron depending on θ_0 , the phase between the wave and the electron. [Show Bortnik
2008 plot?](#) The expression in Eq. 1.21 is commonly referred to as the resonance
 255 condition and is more generally written as
 256

$$\omega - k_{||}v_{||} = \frac{n\Omega_e}{\gamma} \quad (1.22)$$

257 where n is the resonance order, and γ is the relativistic correction (e.g. Millan and
 258 Thorne, 2007). In the case of the cyclotron resonance, $\omega \approx \Omega_e$ thus J_1 is violated.
 259 Since J_1 is violated, J_2 and J_3 are also violated since the conditions required to
 260 violate J_2 and J_3 are less stringent than J_1 . It is important to remember that along
 261 the particle's orbit it will encounter and experience the effects of many waves along
 262 its orbit. The typical MLT extent of a handful of waves that are capable of resonating
 263 with radiation belt electrons are shown in Fig. 1.10.

264 Particle Losses

265 Now that we have seen two general mechanisms with which particles are
 266 accelerated and transported in the magnetosphere, we will now consider a few
 267 specific mechanisms with which particles are lost to the atmosphere or the solar

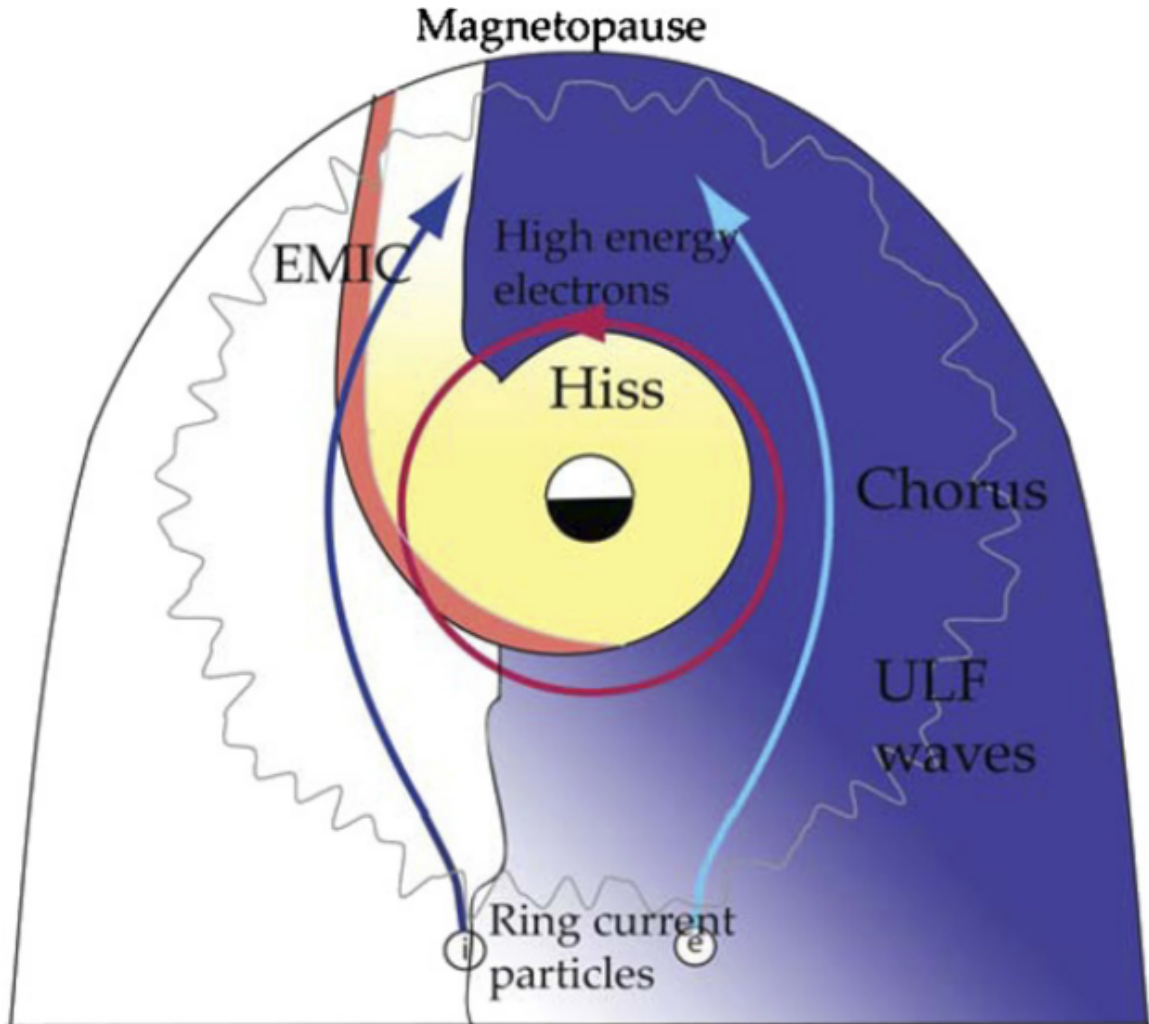


Figure 1.10: Various wave modes in the magnetosphere. Ultra low frequency waves occur through the magnetosphere. Chorus waves are typically observed in the 0-12 midnight-dawn region. EMIC waves are typically observed in the dusk MLT sector. Hiss waves are observed inside the plasmasphere. Figure from Millan and Thorne (2007).

wind. One particle loss mechanisms into the solar wind is magnetopause shadowing (e.g. Ukhorskiy et al., 2006). Particles are sometimes lost when the ring current is strengthened and Earth's magnetic field strength is increased outside of the ring current (and reduced on Earth's surface). If the time scale of the ring current strengthening is slower than a particle drift, J_3 is conserved. Then in order to conserve J_3 while the magnetic field strength is increased, the particle's drift shell must move outward to conserve the magnetic flux contained by the drift shell. Then if the particle's drift shell expands to the point that it crosses the magnetopause, the particle will be lost to the solar wind.

Another particle loss (and acceleration) mechanism is driven by ultra low frequency (ULF) waves and is called radial diffusion. Radial diffusion is the transport of particles from high to low phase space density, f . If the transport is radially inward, particles will appear to be accelerated. On the other hand, radially outward radial diffusion can transport particles through the magnetopause where they will be lost to the solar wind. Reeves et al. (2013) investigated the driver of particle acceleration during the October 2012 storm and observationally found that inward radial diffusion was not dominant, rather local acceleration via wave-resonance heating (i.e. particle diffusion in pitch angle and energy which will be described below) appeared to be the dominant acceleration mechanism.

The loss mechanism central to this dissertation is pitch angle and energy scattering of electrons by waves. Some of the waves that scatter electrons in energy and pitch angle in the inner magnetosphere are: plasmaspheric hiss (e.g. Breneman et al., 2015; O'Brien et al., 2014), EMIC waves (e.g. Capannolo et al., 2019; Hendry et al., 2017), and chorus waves (e.g. Breneman et al., 2017; Kasahara et al., 2018; Ozaki et al., 2019). These wave-particle interactions occur when the resonance condition in Eq. 1.22 is satisfied at which point the particle's energy and α is modified

294 by the wave. More details regarding the theory of pitch angle and energy diffusion is
 295 given in Chapter X. If the wave changes α towards 0 such that $\alpha < \alpha_{LC}$, the particle's
 296 mirror point lowers to less than 100 km altitude where the particle can be lost due
 297 to collisions with air. One manifestation of pitch angle scattering of particles into the
 298 loss cone are microbursts: a sub-second duration impulse of electrons.

299

Microbursts

300 Microbursts were first found in high altitude balloon measurements of bremsstrahlung
 301 X-rays emitted by microburst electrons impacting the atmosphere by Anderson
 302 and Milton (1964). In the following years, numerous balloon flights expanded our
 303 knowledge of non-relativistic microbursts (relativistic microbursts have not yet been
 304 observed by high altitude balloons) by quantifying the microburst spatial extent,
 305 temporal width, occurrence frequency, extent in L and MLT, and their source (a
 306 local plasma instability vs. a propagating disturbance in the magnetosphere) (e.g.
 307 Barcus et al., 1966; Brown et al., 1965; Parks, 1967; Trefall et al., 1966). Since then,
 308 non-relativistic and relativistic (> 500 keV) microbursts electrons have been directly
 309 observed in LEO with spacecraft including the Solar Anomalous and Magnetospheric
 310 Particle Explorer (SAMPEX) (e.g. Blake et al., 1996; Blum et al., 2015; Douma et al.,
 311 2019, 2017; Greeley et al., 2019; Lorentzen et al., 2001a,b; Nakamura et al., 1995, 2000;
 312 O'Brien et al., 2004, 2003), Montana State University's (MSU) Focused Investigation
 313 of Relativistic Electron Bursts: Intensity, Range, and Dynamics II (FIREBIRD-II)
 314 (Anderson et al., 2017; Breneman et al., 2017; Crew et al., 2016; Klumpar et al.,
 315 2015; Spence et al., 2012), and Science Technologies Satellite (STSAT-I) (e.g. Lee
 316 et al., 2012, 2005). An example microburst time series is shown in Fig. 1.11 and was
 317 observed by the FIREBIRD-II CubeSats. The prominent features of the example
 318 microbursts in Fig. 1.11 are their < 1 second duration, half order of magnitude

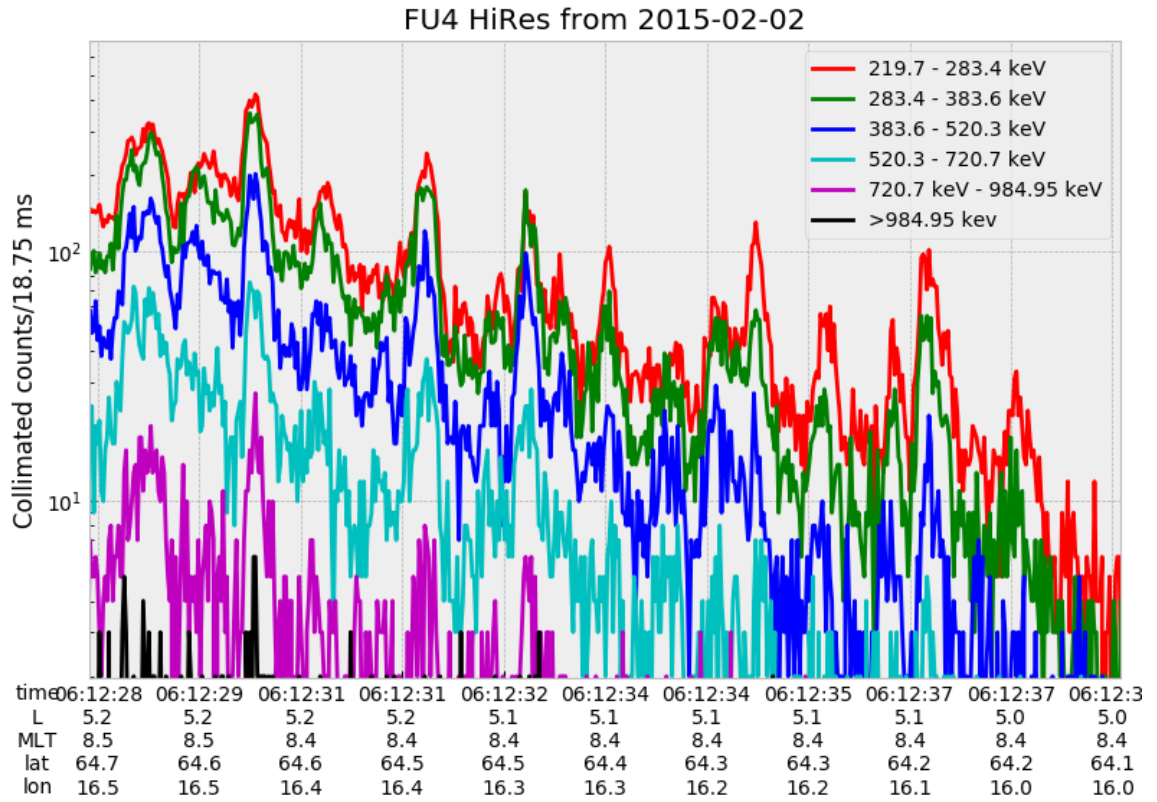


Figure 1.11: An example train of microbursts observed by FIREBIRD-II unit 4 on February 2nd, 2015. The colored curves show the differential energy channel count rates in six channels from ≈ 200 keV to greater than 1 MeV. The x-axis labels show auxiliary information such as time of observation and the spacecraft position in L, MLT, latitude and longitude coordinates.

319 increase in count rate above the falling background, and their approximately 200-800
 320 keV energy extent.

321 Microbursts are observed on magnetic field footprints that are connected to the
 322 outer radiation belt (approximately $4 < L < 8$), and are predominately observed in
 323 the 0-12 MLT sector with an elevated occurrence frequency during magnetospherically
 324 disturbed times as shown in Fig. 1.12 (e.g. Douma et al., 2017). O'Brien et al. (2003)
 325 used SAMPEX relativistic electron data and found that microbursts predominately

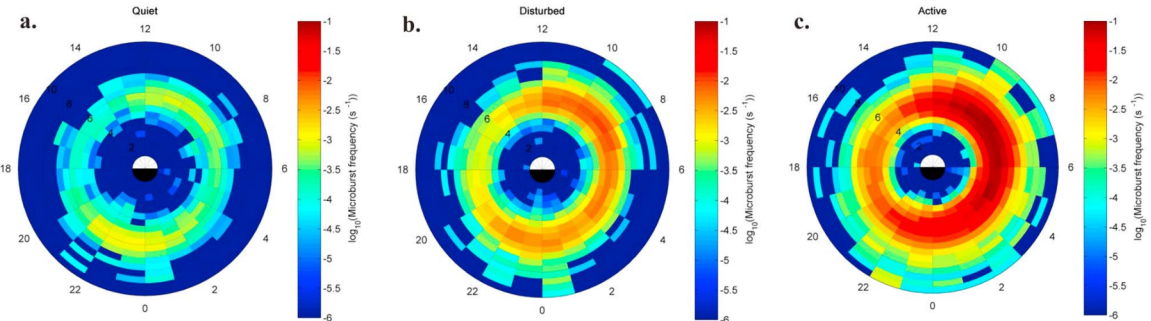


Figure 1.12: Relativistic ($> 1\text{MeV}$) distribution of microburst occurrence rates as a function of L and MLT. The three panels show the microburst occurrence rate dependence on geomagnetic activity, parameterized by the auroral electrojet (AE) index for (a) $\text{AE} < 100 \text{ nT}$, (b) $100 < \text{AE} < 300 \text{ nT}$ and (c) $\text{AE} > 300 \text{ nT}$. Figure from Douma et al. (2017).

326 occur during the main phase of storms, with a heightened occurrence rate during the
 327 recovery phase. Microburst occurrence rates also appear to be higher during high
 328 solar wind velocity events e.g. from co-rotating interaction regions (Greeley et al.,
 329 2019; O'Brien et al., 2003).

330 The impact of microbursts on atmospheric chemistry has been estimated to be
 331 significant. Relativistic microburst electrons impacting the atmosphere are ionized at
 332 $< 100 \text{ km}$ altitudes, with higher energy electrons penetrating closer to the surface.
 333 The resulting chemical reaction of microburst electrons impacting the atmosphere
 334 produces odd hydrogen HO_x and odd nitrogen NO_x molecules. These molecules are
 335 partially responsible for destroying ozone (O_3). Seppälä et al. (2018) modeled a six
 336 hour relativistic microburst storm and found that the mesospheric ozone was reduced
 337 by 7 – 12% in the summer months and 12 – 20% in the winter months.

338 Furthermore, microbursts have also been estimated to have a significant impact
 339 on the outer radiation belt electrons. Radiation belt electron loss due to microbursts
 340 has been estimated to be on the order of a day (Breneman et al., 2017; Douma
 341 et al., 2019; Lorentzen et al., 2001b; O'Brien et al., 2004; Thorne et al., 2005).

342 The wave-particle interactions responsible for generating microbursts are also
 343 believed to accelerate electrons in the radiation belts. As mentioned earlier, when
 344 an electron is in resonance with a wave, energy is exchanged with the wave and
 345 the electron is either accelerated or decelerated. The signature of wave-particle
 346 acceleration been observed for radiation belt electrons (e.g. Horne et al., 2005;
 347 Meredith et al., 2002; Reeves et al., 2013). O'Brien et al. (2003) presented evidence
 348 that enhancements in chorus waves, microbursts, and radiation belt electrons are
 349 related. O'Brien et al. (2003) proposed an explanation where microburst precipitation
 350 is a side effect of electron acceleration due to chorus waves. The widely used
 351 theoretical framework to model interactions between electrons and chorus waves is
 352 quasi-linear diffusion (e.g. Horne et al., 2005; Meredith et al., 2002; Summers, 2005;
 353 Summers et al., 1998; Thorne et al., 2005; Walker, 1993) which is derived in Chapter
 354 ???. Qualitatively, when a particle is resonant with a wave it can be transported in
 355 pitch angle towards the loss cone and lose energy to the wave. In contrast, if the
 356 particle is transported away from the loss cone, it gains energy from the wave.

357 The range of observed microburst energies range from a few tens of keV (e.g.
 358 Datta et al., 1997; Parks, 1967) to greater than 1 MeV (e.g. Blake et al., 1996; Greeley
 359 et al., 2019). The microburst electron flux (J) falls off in energy, and the microburst
 360 energy spectra is typically well fit to a decaying exponential

$$J(E) = J_0 e^{-E/E_0} \quad (1.23)$$

361 where J_0 is the flux at 0 keV (unphysical free parameter) and E_0 quantifies the
 362 efficiency of the scattering mechanism in energy (.e.g Datta et al., 1997; Lee et al.,
 363 2005; Parks, 1967). A small E_0 suggests that mostly low energy particles are scattered
 364 and a high E_0 suggests that the scattering mechanism scatters low and high energy

365 electrons. Reality is a bit more messy and a high E_0 may be a signature of a scattering
366 mechanism preferential to high energy electrons, but is hidden by the convolution of
367 the source particles available to be scattered (typically with a falling energy spectrum)
368 and the energy-dependent scattering efficiency.

369 The short duration of microbursts observed by a single LEO satellite has an
370 ambiguity when interpreting what is exactly a microburst. The two possible realities
371 are: a microburst is very small and spatially stationary so that the LEO spacecraft
372 passes through it in less than a second. Alternatively, microbursts are spatially large
373 with a short duration such that the microburst passes by the spacecraft in a fraction
374 of a second. There are a few ways to distinguish between the two possible realities,
375 and each one has a unique set of advantages.

376 A high altitude balloon provides essentially a stationary view of the precipitating
377 particles under the radiation belt footprints so a short-lived, temporal microburst can
378 be unambiguously identified. Spatial structures, on the other hand, are difficult to
379 identify because a balloon is essentially still on drift timescales.

380 Multi-spacecraft missions are an alternate solution which can determine if a
381 microburst-like feature is spatial or temporal. As will be shown in this dissertation,
382 if a microburst is observed simultaneously by two spacecraft then it is temporal and
383 has a size greater than the spacecraft separation. On the contrary, if two spacecraft
384 observe a microburst-like feature at different times, but at the same location, then
385 the feature is spatial and may be a curtain (Blake and O'Brien, 2016). Both balloon
386 and multi-spacecraft observational methods have a unique set of strengths, and this
387 dissertation takes the multi-spacecraft approach to identify and study microbursts.

Scope of Reserach

389 This dissertation furthers our understanding of the microburst scattering
390 mechanism by observing the scattering directly, and measuring the microburst sizes
391 and comparing them to the size of waves near the magnetic equator where those
392 electrons could have been scattered. Chapter ?? describes a microburst scattering
393 event observed by NASA's Van Allen Probes which was studied in the theoretic
394 framework of pitch angle and energy diffusion. The following two chapters will then
395 study the size of microbursts. Chapter ?? describes a bouncing packet microburst
396 observation made by MSU's FIREBIRD-II mission where the microburst's lower
397 bound longitudinal and latitudinal sizes were estimated. Then Chapter ?? expands
398 the case study from Ch. ?? to a statistical study of microburst sizes using The
399 Aerospace Corporation's AeroCube-6 (AC6) CubeSats. In this study, a Monte Carlo
400 and analytic microburst size models were developed to account for the compounding
401 effects of random microburst sizes and locations. Lastly, Chapter ?? will summarize
402 the dissertation work and make concluding remarks regarding outstanding questions
403 in microburst physics.

Bibliography

- 405 Anderson, B., Shekhar, S., Millan, R., Crew, A., Spence, H., Klumpar, D., Blake, J.,
 406 O'Brien, T., and Turner, D. (2017). Spatial scale and duration of one microburst
 407 region on 13 August 2015. *Journal of Geophysical Research: Space Physics*.
- 408 Anderson, K. A. and Milton, D. W. (1964). Balloon observations of X rays in the
 409 auroral zone: 3. High time resolution studies. *Journal of Geophysical Research*,
 410 69(21):4457–4479.
- 411 Barcus, J., Brown, R., and Rosenberg, T. (1966). Spatial and temporal character of
 412 fast variations in auroral-zone x rays. *Journal of Geophysical Research*, 71(1):125–
 413 141.
- 414 Baumjohann, W. and Treumann, R. A. (1997). *Basic space plasma physics*. World
 415 Scientific.
- 416 Blake, J.,Looper, M., Baker, D., Nakamura, R., Klecker, B., and Hovestadt, D.
 417 (1996). New high temporal and spatial resolution measurements by sampex of the
 418 precipitation of relativistic electrons. *Advances in Space Research*, 18(8):171 – 186.
- 419 Blake, J. B. and O'Brien, T. P. (2016). Observations of small-scale latitudinal
 420 structure in energetic electron precipitation. *Journal of Geophysical Research: Space
 421 Physics*, 121(4):3031–3035. 2015JA021815.
- 422 Blum, L., Li, X., and Denton, M. (2015). Rapid MeV electron precipitation as
 423 observed by SAMPEX/HILT during high-speed stream-driven storms. *Journal of
 424 Geophysical Research: Space Physics*, 120(5):3783–3794. 2014JA020633.
- 425 Breneman, A., Crew, A., Sample, J., Klumpar, D., Johnson, A., Agapitov, O.,
 426 Shumko, M., Turner, D., Santolik, O., Wygant, J., et al. (2017). Observations
 427 directly linking relativistic electron microbursts to whistler mode chorus: Van allen
 428 probes and FIREBIRD II. *Geophysical Research Letters*.
- 429 Breneman, A. W., Halford, A., Millan, R., McCarthy, M., Fennell, J., Sample, J.,
 430 Woodger, L., Hospodarsky, G., Wygant, J. R., Cattell, C. A., et al. (2015). Global-
 431 scale coherence modulation of radiation-belt electron loss from plasmaspheric hiss.
 432 *Nature*, 523(7559):193.
- 433 Brown, R., Barcus, J., and Parsons, N. (1965). Balloon observations of auroral zone
 434 x rays in conjugate regions. 2. microbursts and pulsations. *Journal of Geophysical
 435 Research (U.S.)*.
- 436 Capannolo, L., Li, W., Ma, Q., Shen, X.-C., Zhang, X.-J., Redmon, R., Rodriguez,
 437 J., Engebretson, M., Kletzing, C., Kurth, W., et al. (2019). Energetic electron
 438 precipitation: multi-event analysis of its spatial extent during emic wave activity.
 439 *Journal of Geophysical Research: Space Physics*.

- 440 Claudepierre, S., O'Brien, T.,Looper, M., Blake, J., Fennell, J., Roeder, J.,
 441 Clemmons, J., Mazur, J., Turner, D., Reeves, G., et al. (2019). A revised look
 442 at relativistic electrons in the earth's inner radiation zone and slot region. *Journal*
 443 *of Geophysical Research: Space Physics*, 124(2):934–951.
- 444 Crew, A. B., Spence, H. E., Blake, J. B., Klumpar, D. M., Larsen, B. A., O'Brien,
 445 T. P., Driscoll, S., Handley, M., Legere, J., Longworth, S., Mashburn, K.,
 446 Mosleh, E., Ryhajlo, N., Smith, S., Springer, L., and Widholm, M. (2016). First
 447 multipoint in situ observations of electron microbursts: Initial results from the
 448 NSF FIREBIRD II mission. *Journal of Geophysical Research: Space Physics*,
 449 121(6):5272–5283. 2016JA022485.
- 450 Datta, S., Skoug, R., McCarthy, M., and Parks, G. (1997). Modeling of microburst
 451 electron precipitation using pitch angle diffusion theory. *Journal of Geophysical*
 452 *Research: Space Physics*, 102(A8):17325–17333.
- 453 Douma, E., Rodger, C., Blum, L., O'Brien, T., Clilverd, M., and Blake, J. (2019).
 454 Characteristics of relativistic microburst intensity from sampex observations.
 455 *Journal of Geophysical Research: Space Physics*.
- 456 Douma, E., Rodger, C. J., Blum, L. W., and Clilverd, M. A. (2017). Occurrence
 457 characteristics of relativistic electron microbursts from SAMPEX observations.
 458 *Journal of Geophysical Research: Space Physics*, 122(8):8096–8107. 2017JA024067.
- 459 Eastwood, J., Hietala, H., Toth, G., Phan, T., and Fujimoto, M. (2015). What
 460 controls the structure and dynamics of earths magnetosphere? *Space Science*
 461 *Reviews*, 188(1-4):251–286.
- 462 Greeley, A., Kanekal, S., Baker, D., Klecker, B., and Schiller, Q. (2019). Quantifying
 463 the contribution of microbursts to global electron loss in the radiation belts. *Journal*
 464 *of Geophysical Research: Space Physics*.
- 465 Hendry, A. T., Rodger, C. J., and Clilverd, M. A. (2017). Evidence of sub-mev
 466 emic-driven electron precipitation. *Geophysical Research Letters*, 44(3):1210–1218.
- 467 Horne, R., Glauert, S., Meredith, N., Boscher, D., Maget, V., Heynderickx, D., and
 468 Pitchford, D. (2013). Space weather impacts on satellites and forecasting the earth's
 469 electron radiation belts with spacecast. *Space Weather*, 11(4):169–186.
- 470 Horne, R. B., Thorne, R. M., Shprits, Y. Y., Meredith, N. P., Glauert, S. A., Smith,
 471 A. J., Kanekal, S. G., Baker, D. N., Engebretson, M. J., Posch, J. L., et al.
 472 (2005). Wave acceleration of electrons in the van allen radiation belts. *Nature*,
 473 437(7056):227.
- 474 Kasahara, S., Miyoshi, Y., Yokota, S., Mitani, T., Kasahara, Y., Matsuda, S.,
 475 Kumamoto, A., Matsuoka, A., Kazama, Y., Frey, H., et al. (2018). Pulsating
 476 aurora from electron scattering by chorus waves. *Nature*, 554(7692):337.

- 477 Klumpar, D., Springer, L., Mosleh, E., Mashburn, K., Berardinelli, S., Gunderson,
 478 A., Handly, M., Ryhajlo, N., Spence, H., Smith, S., Legere, J., Widholm, M.,
 479 Longworth, S., Crew, A., Larsen, B., Blake, J., and Walmsley, N. (2015). Flight
 480 system technologies enabling the twin-cubesat firebird-ii scientific mission.
- 481 Lee, J. J., Parks, G. K., Lee, E., Tsurutani, B. T., Hwang, J., Cho, K. S., Kim, K.-H.,
 482 Park, Y. D., Min, K. W., and McCarthy, M. P. (2012). Anisotropic pitch angle
 483 distribution of 100 keV microburst electrons in the loss cone: measurements from
 484 STSAT-1. *Annales Geophysicae*, 30(11):1567–1573.
- 485 Lee, J.-J., Parks, G. K., Min, K. W., Kim, H. J., Park, J., Hwang, J., McCarthy,
 486 M. P., Lee, E., Ryu, K. S., Lim, J. T., Sim, E. S., Lee, H. W., Kang, K. I., and
 487 Park, H. Y. (2005). Energy spectra of 170–360 keV electron microbursts measured
 488 by the korean STSAT-1. *Geophysical Research Letters*, 32(13). L13106.
- 489 Li, X., Selesnick, R., Schiller, Q., Zhang, K., Zhao, H., Baker, D. N., and Temerin,
 490 M. A. (2017). Measurement of electrons from albedo neutron decay and neutron
 491 density in near-earth space. *Nature*, 552(7685):382.
- 492 Lorentzen, K. R., Blake, J. B., Inan, U. S., and Bortnik, J. (2001a). Observations
 493 of relativistic electron microbursts in association with VLF chorus. *Journal of
 494 Geophysical Research: Space Physics*, 106(A4):6017–6027.
- 495 Lorentzen, K. R.,Looper, M. D., and Blake, J. B. (2001b). Relativistic electron
 496 microbursts during the GEM storms. *Geophysical Research Letters*, 28(13):2573–
 497 2576.
- 498 Lyons, L. R. and Thorne, R. M. (1973). Equilibrium structure of radiation belt
 499 electrons. *Journal of Geophysical Research*, 78(13):2142–2149.
- 500 Meredith, N., Horne, R., Summers, D., Thorne, R., Iles, R., Heynderickx, D., and
 501 Anderson, R. (2002). Evidence for acceleration of outer zone electrons to relativistic
 502 energies by whistler mode chorus. In *Annales Geophysicae*, volume 20, pages 967–
 503 979.
- 504 Millan, R. and Thorne, R. (2007). Review of radiation belt relativistic electron losses.
 505 *Journal of Atmospheric and Solar-Terrestrial Physics*, 69(3):362 – 377.
- 506 Nakamura, R., Baker, D. N., Blake, J. B., Kanekal, S., Klecker, B., and Hovestadt,
 507 D. (1995). Relativistic electron precipitation enhancements near the outer edge of
 508 the radiation belt. *Geophysical Research Letters*, 22(9):1129–1132.
- 509 Nakamura, R., Isowa, M., Kamide, Y., Baker, D., Blake, J., and Looper, M. (2000).
 510 Observations of relativistic electron microbursts in association with VLF chorus.
 511 *J. Geophys. Res.*, 105:15875–15885.

- 512 O'Brien, T., Claudepierre, S., Blake, J., Fennell, J. F., Clemons, J., Roeder, J.,
 513 Spence, H. E., Reeves, G., and Baker, D. (2014). An empirically observed pitch-
 514 angle diffusion eigenmode in the earth's electron belt near $l^* = 5.0$. *Geophysical*
 515 *Research Letters*, 41(2):251–258.
- 516 O'Brien, T., Claudepierre, S., Guild, T., Fennell, J., Turner, D., Blake, J., Clemons,
 517 J., and Roeder, J. (2016). Inner zone and slot electron radial diffusion revisited.
 518 *Geophysical Research Letters*, 43(14):7301–7310.
- 519 O'Brien, T. and Moldwin, M. (2003). Empirical plasmapause models from magnetic
 520 indices. *Geophysical Research Letters*, 30(4).
- 521 O'Brien, T. P.,Looper, M. D., and Blake, J. B. (2004). Quantification of relativistic
 522 electron microburst losses during the GEM storms. *Geophysical Research Letters*,
 523 31(4). L04802.
- 524 O'Brien, T. P., Lorentzen, K. R., Mann, I. R., Meredith, N. P., Blake, J. B., Fennell,
 525 J. F., Looper, M. D., Milling, D. K., and Anderson, R. R. (2003). Energization of
 526 relativistic electrons in the presence of ULF power and MeV microbursts: Evidence
 527 for dual ULF and VLF acceleration. *Journal of Geophysical Research: Space*
 528 *Physics*, 108(A8).
- 529 Ozaki, M., Miyoshi, Y., Shiokawa, K., Hosokawa, K., Oyama, S.-i., Kataoka, R.,
 530 Ebihara, Y., Ogawa, Y., Kasahara, Y., Yagitani, S., et al. (2019). Visualization of
 531 rapid electron precipitation via chorus element wave–particle interactions. *Nature*
 532 *communications*, 10(1):257.
- 533 Parks, G. K. (1967). Spatial characteristics of auroral-zone X-ray microbursts. *Journal*
 534 *of Geophysical Research*, 72(1):215–226.
- 535 Reeves, G., Spence, H. E., Henderson, M., Morley, S., Friedel, R., Funsten, H., Baker,
 536 D., Kanekal, S., Blake, J., Fennell, J., et al. (2013). Electron acceleration in the
 537 heart of the van allen radiation belts. *Science*, 341(6149):991–994.
- 538 Reeves, G. D., McAdams, K. L., Friedel, R. H. W., and O'Brien, T. P. (2003). Ac-
 539 celeration and loss of relativistic electrons during geomagnetic storms. *Geophysical*
 540 *Research Letters*, 30(10):n/a–n/a. 1529.
- 541 Schulz, M. and Lanzerotti, L. J. (1974). *Particle Diffusion in the Radiation Belts*.
 542 Springer.
- 543 Seppälä, A., Douma, E., Rodger, C., Verronen, P., Clilverd, M. A., and Bortnik, J.
 544 (2018). Relativistic electron microburst events: Modeling the atmospheric impact.
 545 *Geophysical Research Letters*, 45(2):1141–1147.

- 546 Spence, H. E., Blake, J. B., Crew, A. B., Driscoll, S., Klumpar, D. M., Larsen,
 547 B. A., Legere, J., Longworth, S., Mosleh, E., O'Brien, T. P., Smith, S., Springer,
 548 L., and Widholm, M. (2012). Focusing on size and energy dependence of electron
 549 microbursts from the van allen radiation belts. *Space Weather*, 10(11).
- 550 Summers, D. (2005). Quasi-linear diffusion coefficients for field-aligned electro-
 551 magnetic waves with applications to the magnetosphere. *Journal of Geophysical
 552 Research: Space Physics*, 110(A8):n/a–n/a. A08213.
- 553 Summers, D., Thorne, R. M., and Xiao, F. (1998). Relativistic theory of wave-particle
 554 resonant diffusion with application to electron acceleration in the magnetosphere.
 555 *Journal of Geophysical Research: Space Physics*, 103(A9):20487–20500.
- 556 Thorne, R. M., O'Brien, T. P., Shprits, Y. Y., Summers, D., and Horne, R. B. (2005).
 557 Timescale for MeV electron microburst loss during geomagnetic storms. *Journal
 558 of Geophysical Research: Space Physics*, 110(A9). A09202.
- 559 Trefall, H., Bjordal, J., Ullaland, S., and Stadsnes, J. (1966). On the extension of
 560 auroral-zone x-ray microbursts. *Journal of Atmospheric and Terrestrial Physics*,
 561 28(2):225–233.
- 562 Tsurutani, B. T. and Lakhina, G. S. (1997). Some basic concepts of wave-particle
 563 interactions in collisionless plasmas. *Reviews of Geophysics*, 35(4):491–501.
- 564 Ukhorskiy, A. Y., Anderson, B. J., Brandt, P. C., and Tsyganenko, N. A. (2006).
 565 Storm time evolution of the outer radiation belt: Transport and losses. *Journal of
 566 Geophysical Research: Space Physics*, 111(A11):n/a–n/a. A11S03.
- 567 Van Allen, J. A. (1959). The geomagnetically trapped corpuscular radiation. *Journal
 568 of Geophysical Research*, 64(11):1683–1689.
- 569 Vernov, S. and Chudakov, A. (1960). Investigation of radiation in outer space. In
 570 *International Cosmic Ray Conference*, volume 3, page 19.
- 571 Walker, A. D. M. (1993). *Plasma waves in the magnetosphere*, volume 24. Springer
 572 Science & Business Media.